

Causal Network Discovery from Interventional Count Data with Latent Linear DAGs

Yijiao Zhang and Hongzhe Li *

Department of Biostatistics, Epidemiology and Informatics
University of Pennsylvania

Abstract

The increasing availability of interventional data offers new opportunities for causal discovery, with gene perturbation studies providing a prominent example. Such data are typically count-valued and subject to substantial measurement error arising from technical variability and latent state heterogeneity. Motivated by these challenges, we study identification and estimation in latent linear structural causal models for interventional count data. We propose a latent linear Gaussian directed acyclic graph (DAG) model with Poisson measurement error that explicitly separates the latent causal structure from the observed counts. Under a mean-shift intervention design, we establish population-level identifiability of the latent causal DAG. Building on these identification results, we develop an estimation procedure based on sparse inverse matrix estimation and provide theoretical guarantees on estimation error and finite-sample causal discovery. Simulation studies and applications to Perturb-seq data demonstrate the practical effectiveness of the proposed method.

Keywords: Causal discovery; Measurement error; Poisson model; Perturb-seq data.

*Corresponding author. Yijiao Zhang is a postdoctoral fellow and Hongzhe Li is Perelman Professor in the Department of Biostatistics, Epidemiology and Informatics at the University of Pennsylvania.

1 Introduction

Understanding causal relationships among variables is a central problem across many scientific disciplines, including biology, medicine, and economics. Directed acyclic graphs (DAGs) provide a widely used framework for representing causal systems. However, observational data alone are generally insufficient to identify the underlying causal DAG. In general, they determine only a Markov equivalence class, within which the directions of edges that are crucial for causal interpretation are not uniquely identifiable.

The increasing availability of interventional data offers new opportunities for identifying causal graphs. A prominent example arises in gene regulatory network inference, where recent CRISPR-based perturbation technologies (Shalem et al., 2014) have enabled Perturb-seq experiments that combine pooled gene perturbations with single-cell RNA sequencing, yielding high-throughput interventional expression data with known targets at single-cell resolution (Replogle et al., 2022). This experimental design provides rich interventional information for studying causal regulatory relationships.

Despite these advantages, analyzing Perturb-seq data poses several substantial challenges. First, gene expression measurements in single-cell perturbation experiments are inherently count-valued, reflecting sequencing read counts rather than continuous expression levels. Most existing interventional causal discovery methods rely on Gaussian or continuous approximations and are therefore not well suited for such data. Additionally, observed counts exhibit substantial technical noise, arising from library size effects and experimental batch effects, which induces non-negligible measurement error relative to the underlying latent expression. Ignoring this measurement structure can lead to biased inference and misleading causal conclusions (Zhang et al., 2018; Sarkar and Stephens, 2021), yet it is rarely addressed in existing interventional methods.

Moreover, Perturb-seq data may exhibit unmeasured confounding arising from latent cellular states and shared regulatory programs, which can simultaneously influence multiple genes. Such latent confounding induces spurious dependencies among genes and violates the causal sufficiency or independent noise assumptions commonly adopted by existing interventional causal discovery methods, potentially leading to biased DAG structure learning.

Furthermore, in Perturb-seq experiments, the number of cells available for each individual perturbation is often limited. In contrast, identifiability results for many interventional-data-based methods are typically established under infinite-sample assumptions, and their practical performance relies on stable estimation of score functions. Such estimation becomes particularly unstable in high-dimensional settings with small per-intervention sample sizes, limiting the applicability of existing methods to realistic Perturb-seq data.

Our contribution Motivated by these considerations, we focus on the problem of identification and estimation of latent linear causal DAG models for interventional count data with measurement errors. Our main contributions are threefold.

Methodologically, we propose a latent linear Gaussian DAG model with Poisson measurement error, which decouples the causal structure among latent expression levels from the observed measurement process. Under a mean-shift intervention design in which each gene is perturbed at least once, we establish population-level identifiability of the latent causal DAG. Our identification results do not rely on the causal faithfulness assumption, which can be restricted in high-dimensions (Uhler et al., 2013). The proposed method works under soft interventions and allow for the presence of latent confounding.

Computationally, building on these identifiability results, we develop a new estimation procedure for the latent causal coefficient matrix that integrates ideas from sparse inverse matrix estimation with explicit DAG constraints. The resulting optimization problem is

efficiently solved using the alternating direction method of multipliers.

Theoretically, we derive non-asymptotic estimation error bounds for the proposed estimator of the causal coefficient matrix. Under a beta-min type condition on the interventional strength and signal strength on the true edges, we characterize the finite-sample DAG discovery rate and quantify the probability of exact DAG recovery.

Related Work Below, we provide a non-exhaustive review of the most closely related work on causal discovery. For more comprehensive surveys, see (Heinze-Deml et al., 2018; Squires and Uhler, 2023).

Causal discovery from observational data has been extensively studied via *constraint-based* and *score-based* methods. *Constraint-based* methods, such as the PC algorithm (Spirtes et al., 2000), rely on conditional independence testing and typically rely on strong faithfulness assumptions. *Score-based* methods formulate DAG learning as the optimization of a scoring function, ranging from greedy search (Chickering, 2002) to continuous optimization (Zheng et al., 2018b; Bello et al., 2022). These approaches avoid faithfulness assumptions and instead require beta-min conditions for consistent recovery (van de Geer and Bühlmann, 2013). Purely observational data identify a Markov equivalence class, unless additional distributional assumptions are imposed, such as non-gaussian errors (Shimizu et al., 2006) or equal error variances (Peters and Bühlmann, 2014).

Interventional data provide information to break Markov equivalence and enable full DAG identification. When interventional targets are known, Hauser and Bühlmann (2012) proposed a score-based approach that identifies DAGs up to an interventional Markov equivalence class. Wang et al. (2017) developed a hybrid method that alternates between structure optimization and conditional independence testing, while Xue et al. (2025) extended continuous score-based optimization to interventional settings. These methods do

not allow latent confounding and rely on *hard* interventions, under which the dependence of the intervention target on its parents is removed. Related work considering unknown intervention targets includes (Squires et al., 2020; Li et al., 2025; Varici et al., 2025).

Several lines of works study causal discovery with latent confounding. A classical line of work studies causal discovery over acyclic directed mixed graphs (ADMGs), which encode conditional independence on the observed margin. Representative approaches include constraint-based methods such as FCI and its variants (Spirtes et al., 2000; Colombo et al., 2012), score-based methods based on continuous optimization (Bhattacharya et al., 2021), and approaches exploiting non-Gaussianity (Wang and Drton, 2023). Another line of work imposes structured assumptions on the error covariance and performs deconfounding through precision matrix decomposition (Frot et al., 2019; Pal et al., 2025). Our method accommodates latent confounding without explicitly modeling the confounding effects.

Most existing methods are not tailored to count-valued data. Several works study causal discovery for observational Poisson models (Park and Raskutti, 2015; Park and Park, 2019) and zero-inflated Poisson models (Choi and Ni, 2023), but they do not account for latent confounding or measurement error. A smaller body of work considers DAG learning in the presence of measurement error (Zhang et al., 2018; Dai et al., 2022; Saeed et al., 2020), which is largely constraint-based and restricted to observational settings.

Organization The remainder of the paper is organized as follows. We introduce the model, identifiability results, and estimation procedure in Sections 2 - 4. Section 5 develops theoretical guarantees, including estimation error bounds and finite-sample DAG identification results. Simulation studies are reported in Section 6, followed by real data applications in Section 7. Section 8 concludes with a discussion.

2 Statistical Model for Perturb-seq Single Cell RNA-seq Data

We first introduce some basic notations. Denote $[p] = 1, \dots, p$. For a matrix $B = (B_{jk}) \in \mathbb{R}^{p \times p}$, we define the elementwise max norm $\|B\|_{\max} = \max_{j,k} |B_{jk}|$, the spectral norm $\|B\|_2 = \sup_{\|x\|_2=1} \|Bx\|_2$, matrix ℓ_1 norm $\|B\|_{L_1} = \max_{1 \leq j \leq p} \sum_{i=1}^p |a_{ij}|$, the elementwise ℓ_1 norm $\|B\|_1 = \sum_{i=1}^p \sum_{j=1}^p |a_{ij}|$, and the Frobenius norm $\|B\|_F = (\sum_{j,k} B_{jk}^2)^{1/2}$. We denote by $\|B\|_0$ the number of nonzero entries in B , i.e., $\|B\|_0 = |\{(j, k) : B_{jk} \neq 0\}|$.

We consider gene expression count data collected under multiple interventional environments generated by CRISPR perturbations. Let $X^{(m)} = (X_1^{(m)}, \dots, X_p^{(m)})^\top \in \mathbb{R}^p$ denote the observed gene expression vector in environment $m \in \{0, 1, \dots, M\}$, where $m = 0$ corresponds to the control (non-intervened) condition. Each interventional environment $m > 0$ targets a single gene for perturbation, and we denote by $I^{(m)} = \ell_m \in [p]$ the index of the perturbed gene in environment m .

To separate the measurement process from the underlying expression process in single-cell RNA sequencing data (Sarkar and Stephens, 2021), we model the observed gene expression counts through an explicit measurement layer and a latent expression layer. Specifically, for each environment m , the observed count $X_j^{(m)}$ of gene j is modeled as a Poisson random variable conditional on the library size $L \in \mathbb{R}$, the cell-level covariates $C \in \mathbb{R}^q$, and the latent true expression level $Z_j^{(m)}$:

$$X_j^{(m)} \mid L, C, Z_j^{(m)} \sim \text{Poisson}(L \exp\{s_j(C) + Z_j^{(m)}\}), \quad j = 1, \dots, p. \quad (1)$$

Here, L accounts for sequencing depth, while $s_j(C) \in \mathbb{R}$ captures the systematic effects of observable covariates such as batch effects that may effect the observed sequence counts for gene j . After adjusting for technical effects and observable cell heterogeneity, $Z_j^{(m)}$

represents the latent expression level. We assume that $Z^{(m)} \perp (C, L)$ for all $m \in \{0, \dots, p\}$, implying that the sequencing depth and possible batch effects are independent of the observed sequencing counts.

To characterize the latent causal structure underlying gene expression, we consider a linear Gaussian structural causal model (SCM) on the latent expression vector $Z^{(m)} = (Z_1^{(m)}, \dots, Z_p^{(m)})^\top \in \mathbb{R}^p$ for each environment $m \in \{0, \dots, p\}$. Specifically, we consider

$$Z^{(m)} = AZ^{(m)} + \eta^{(m)} + \varepsilon^{(m)}, \quad \varepsilon^{(m)} \sim \mathcal{N}(0, \Sigma_e^{(m)}), \quad (m = 0, \dots, p), \quad (2)$$

$$\eta^{(m)} = \eta^{(0)} + \alpha_m e_{\ell_m}, \quad (m = 1, \dots, p) \quad (3)$$

where $A \in \mathbb{R}^{p \times p}$ is the causal coefficient matrix, $\eta^{(m)} \in \mathbb{R}^p$ is an environment-specific intercept, $\alpha_m \in \mathbb{R}$ is a scalar and $e_j \in \mathbb{R}^p$ denotes the j -th canonical basis vector. The sample size under the m -th environment is denoted by n_m .

The shared coefficient matrix A in (2) induces a DAG $\mathcal{G} = ([p], \mathcal{E})$ on the vertex set $[p] = \{1, \dots, p\}$, where the edge set is defined as $\mathcal{E} = \{(i, j) : A_{ji} \neq 0\}$. In particular, a nonzero entry A_{ji} corresponds to a directed edge $i \rightarrow j$ in \mathcal{G} . We assume that A is such that \mathcal{G} is acyclic. Thus, A represents the latent causal mechanism and is assumed to be invariant across environments. More generally, for any matrix $A \in \mathbb{R}^{p \times p}$, we denote by $\mathcal{G}(A)$ the directed graph induced by A under this rule.

In addition, model (2) assumes a *mean shift* between the interventional and control environments, captured by the contrast of the intercepts $\eta^{(m)} - \eta^{(0)}$. The exogenous noise $\varepsilon^{(m)}$ is modeled as Gaussian with environment-specific covariance $\Sigma_e^{(m)}$, which may be non-diagonal, allowing possible latent confounding. Equation (3) further imposes a *one-sparse* mean-shift structure: only the intercept of the targeted gene ℓ_m is directly shifted by an amount α_m , where $|\alpha_m|$ quantifies the intervention strength in environment m .

The acyclicity of A means there exists a permutation matrix P (a topological order of

\mathcal{G}) such that $P^\top AP$ is strictly lower triangular. In particular, $I - A$ is invertible and hence we define $B := (I - A)^{-1}$. Under this representation, the latent variables satisfy

$$Z^{(m)} = B\varepsilon^{(m)} + \mu^{(m)}, \quad \mu^{(m)} := \mathbb{E}[Z^{(m)}] = B\eta^{(m)}. \quad (4)$$

Equation (4) shows that the one-sparse shift in $\eta^{(m)}$ can propagate through the causal system and induce dense changes in downstream genes.

We briefly discuss the plausibility of the modeling assumptions above and their connections to the literature. The invariance of A across environments reflects the principle of invariant causal mechanisms under interventions, which is a standard premise in intervention-based causal discovery (Shen et al., 2025; Li et al., 2025).

Mean-shift interventions constitute a class of soft interventions that modify the conditional distribution of an intervened target through shifts in its mean while preserving its dependence on parent variables, and have been widely used in interventional causal discovery (Liu et al., 2025; Li et al., 2025). In contrast, hard or do-interventions commonly assumed in existing interventional causal discovery methods (Hauser and Bühlmann, 2012; Wang et al., 2017; Xue et al., 2025) completely remove the dependence of the target on its parents. Soft interventions are often more realistic in practice, as biological perturbations are typically partial and noisy rather than fully disruptive. The one-sparse form in (3) can be seen as an special case of the so-called ‘sparse mechanism shift hypothesis’ in (Schölkopf et al., 2021) and was similarly used in (Li et al., 2025).

Moreover, the deterministic mean-shift assumption can be generalized to a stochastic mean shift by introducing a random vector $\tilde{\eta}^{(m)} \in \mathbb{R}^p$ with mean $\eta^{(m)}$, possibly allowing mild correlation with the error term. Our theoretical results extend naturally to this setting, since the identification relies only on the first-order moment of $\tilde{\eta}^{(m)}$. This stochastic formulation is more realistic in practice, as it captures heterogeneous perturbation effects

across cells arising from variable perturbation efficiency and incomplete penetrance.

3 Identification of the DAG Under Unmeasured Confounders

Under linear Gaussian SCMs, observational data alone only identify the causal structure up to a Markov equivalence class. By contrast, the invariance of the causal mechanism A across environments, together with mean-shifts in the latent expression model, enables identification of the underlying causal structure through cross-environment mean changes. A key observation is that the mean difference between environment m and the control is

$$\Delta\mu^{(m)} := \mu^{(m)} - \mu^{(0)} = \alpha_m B e_{\ell_m}, \quad (5)$$

which implies that $\Delta\mu^{(m)}$ equals the ℓ_m -th column of B up to a scalar factor. Moreover, under acyclicity, it is easy to verify that $P^\top B P$ is unit lower triangular. This unit-diagonal constraint fixes the scale and sign of each column of B , so that the ℓ_m -th column of B is identifiable from $\Delta\mu^{(m)}$ whenever $\alpha_m \neq 0$. Provided that for each node $\ell \in [p]$ there exists at least one environment m with $\ell_m = \ell$ and $\alpha_m \neq 0$, stacking the recovered columns yields identifiability of B and hence of the causal mechanism A .

It therefore suffices to identify the latent means $\{\mu^{(m)}\}_{m=0}^M$ from the observed data. Under the Poisson–lognormal observation model, moments of the observed counts $X^{(m)}$ admit an explicit mapping to moments of the latent expression variables $Z^{(m)}$. Specifically, letting $S_j(C, L) = L \exp(s_j(C))$, the first- and second-order moments of the scaled counts $Y_j^{(m)} = X_j^{(m)} / S_j(C, L)$ are linked to the moments of the latent Gaussian variable $Z_j^{(m)}$ via

$$\mu_j^{(m)} = \log(\mathbb{E}[Y_j^{(m)}]) - \frac{1}{2} \Sigma_{jj}^{(m)}, \quad (6)$$

where

$$\Sigma_{jj}^{(m)} = \log \left(\frac{\mathbb{E}[Y_j^{(m)}(Y_j^{(m)} - 1)]}{(\mathbb{E}[Y_j^{(m)}])^2} \right).$$

These relationships connect the mean of the latent expression model $\mu^{(m)}$ to the observable moments of the covariate-adjusted scaled counts $\{Y_j^{(m)}\}_{j \in [p]}$. We note that the covariate effect $s_j(C)$ operates solely at the measurement level and remains invariant across environments. As such, it can be regarded as a nuisance that does not affect the identification of the latent causal structure. We then have the following identification results.

Theorem 3.1. *Under the model (1)–(3), the causal mechanism A is identifiable by jointly leveraging observational and interventional data, provided that each node is subject to at least one non-vanishing one-sparse mean-shift intervention in the latent expression model.*

Theorem 3.1 establishes identifiability of the causal mechanism A at the population level by jointly leveraging observational and interventional data. Here, a *non-vanishing* mean-shift intervention refers to a perturbation with mean-shift strength $\alpha_m \neq 0$ in the latent expression model. In finite samples, successful recovery further requires the mean-shift magnitude $|\alpha_m|$ to exceed a problem-dependent lower bound, which depends on factors such as the graph density and the number of interventional samples. A precise characterization of this requirement is provided in Section 5.

Compared with existing methods for causal discovery from interventional data, our framework does not require *hard* or *do*-type interventions as in (Hauser and Bühlmann, 2012; Wang et al., 2017; Xue et al., 2025). DOTEARS (Xue et al., 2025) also considers linear SCMs, but assumes diagonal noise covariance and invariant exogenous variances for non-targeted nodes across environments, whereas our method allows non-diagonal and environment-specific covariance matrices. For observational count data, existing identifiability results either exclude measurement error (Park and Park, 2019) or recover only

Markov equivalence classes (Saeed et al., 2020).

A key distinction is that our framework accommodates latent confounding. In linear structural causal models, latent confounding manifests as correlated errors (Pearl, 2009; Bhattacharya et al., 2021), so in our setting directed edges are encoded in the coefficient matrix A , while bidirected dependence corresponds to nonzero off-diagonal entries of the noise covariance matrix. From the perspective of mixed graphs, Theorem 3.1 shows that the directed edge structure remains identifiable even in the presence of latent confounding. Unlike approaches based on explicit covariance modeling and deconfounding via precision matrix decomposition (Frot et al., 2019; Pal et al., 2025), our method exploits interventional mean shifts and the fact that, under the mean-shift assumption, differences in latent means are unaffected by latent confounding, thus avoiding explicit modeling of the confounding structure and node-wise deconfounding procedures.

4 Estimation of Causal Coefficient Matrix and DAG

Recovery

In this section, we describe the estimation procedure for the causal coefficient matrix A . The procedure consists of four main steps: (i) estimating and removing measurement-layer effects, (ii) mapping observed moments to latent means under the Poisson–lognormal model, (iii) recovering the columns of $B = (I - A)^{-1}$ via cross-environment mean shifts, and (iv) estimating A under sparsity and acyclicity constraints. The complete algorithm is summarized in Algorithm 1.

We begin by estimating the covariate effect $s_j(C)$ in the measurement layer. In practice, $s_j(C)$ can be estimated using a Poisson regression with offset $\log L$ and predictors C .

Specifically, for each gene j , we can estimate the covariate effect $s_j(C)$ using a generalized linear model with log link and offset $\log L$,

$$\log \mathbb{E}[X_{ij}^{(m)} \mid C_i, L_i] = \log L_i + \beta_j^\top C_i + \delta_j^{(m)}, \quad (7)$$

where $\delta_j^{(m)}$ are environment-specific intercepts that capture mean shifts and do not affect identification of β_j . Let $\hat{\beta}_j$ denote the (quasi-)maximum likelihood estimate, and define $\hat{s}_j(C_i) = C_i^\top \hat{\beta}_j$. Using $\hat{s}_j(\cdot)$, we can form the rescaled counts $\hat{Y}_{ij}^{(m)} = X_{ij}^{(m)} / (L_i^{(m)} \exp(\hat{s}_j(C_i^{(m)})))$ from which the latent mean vector $\hat{\mu}^{(m)}$ is obtained by replacing the population expectation $\mathbb{E}[\cdot]$ in (6) with the empirical expectation $\hat{\mathbb{E}}[\cdot]$ as specified in (9).

For each interventional environment $m \in \{1, \dots, p\}$, we compute latent mean contrasts $\Delta \hat{\mu}^{(m)} = \hat{\mu}^{(m)} - \hat{\mu}^{(0)}$ and reconstruct the ℓ -th column of B by $\hat{b}_\ell = \Delta \hat{\mu}^{(m)} / \Delta \hat{\mu}_\ell^{(m)}$ where $l = I^{(m)}$. Collecting these columns yields $\hat{B} = [\hat{b}_1, \dots, \hat{b}_p] \in \mathbb{R}^{p \times p}$.

Finally, to recover the causal matrix A , we estimate a sparse weighted adjacency matrix A under acyclicity constraints. Given the estimate $\hat{B} \approx (I - A)^{-1}$, we consider the constrained optimization problem

$$\hat{A} \in \arg \min_A \|A\|_1 \quad \text{s.t.} \quad h(A) = 0, \quad \|\hat{B}(I - A) - I\|_{\max} \leq \lambda_s, \quad (8)$$

where $h(A) = 0$ enforces the DAG constraint, and the ℓ_∞ constraint controls the approximation error of $\hat{B}(I - A)$ in a CLIME-type regularization framework (Cai et al., 2011).

We include the acyclicity constraint $h(\cdot)$ to ensure that B is unit-diagonal. Typical choices of $h(\cdot)$ include $h(A) = \text{tr}(\exp(A \circ A)) - p$ as in NOTEARS (Zheng et al., 2018b), or $h(A) = -\log |uI - A| + p \log u$ for $u \in \mathbb{R}^u$ as in DAGMA (Bello et al., 2022). To obtain the estimated causal graph, we then apply entrywise hard thresholding to \hat{A} and form the thresholded estimator \hat{A}_τ by $(\hat{A}_\tau)_{ij} := \hat{a}_{ij} \mathbf{1}\{|\hat{a}_{ij}| \geq \tau\}$, for $i, j \in [p]$.

To handle the non-smooth ℓ_∞ constraint, we introduce an auxiliary variable $Z = \hat{B}(I -$

Algorithm 1 PLN-intervn: Causal discovery from interventional Poisson count data

Input: Observed data $\{(X^{(m)}, L^{(m)}, C^{(m)})\}_{m=0}^M$, intervention targets $\{I^{(m)} = \ell_m\}_{m=1}^M$, regularization level λ_s , threshold level $\tau > 0$.

1. **Measurement-layer adjustment:** Obtain $\hat{s}_j(C_i)$ by fitting (7) and compute scaled counts $\hat{Y}_{ij}^{(m)} = X_{ij}^{(m)} / (L_i^{(m)} \exp\{\hat{s}_j(C_i^{(m)})\})$.
2. **Mapping observed moments to latent means:** Compute $\hat{\mu}^{(m)}$ via the transformation of empirical moments via

$$\hat{\mu}_j^{(m)} = \log(\hat{\mathbb{E}}[\hat{Y}_j^{(m)}]) - \frac{1}{2}\hat{\Sigma}_{jj}^{(m)}, \quad \text{where } \hat{\Sigma}_{jj}^{(m)} = \log\left(\frac{\hat{\mathbb{E}}[\hat{Y}_j^{(m)}(\hat{Y}_j^{(m)} - 1)]}{\hat{\mathbb{E}}[\hat{Y}_j^{(m)}]^2}\right). \quad (9)$$

3. **Column recovery of B :** For the environment m targeting $\ell = I^{(m)}$: reconstruct the ℓ -th column of B by $\hat{b}_\ell = \Delta\hat{\mu}^{(m)} / \Delta\hat{\mu}_\ell^{(m)}$. Collect the columns into a matrix to obtain $\hat{B} = [\hat{b}_1, \dots, \hat{b}_p] \in \mathbb{R}^{p \times p}$.
4. **Sparse DAG estimation of A :** Obtain \hat{A} by solving (8).

Output: Estimated causal matrix \hat{A} and recovered graph $\hat{\mathcal{G}} = \mathcal{G}(\hat{A}_\tau)$.

A) $- I$ and rewrite problem (8) equivalently as

$$\min_{A, Z} \|A\|_1 \quad \text{s.t.} \quad Z = \hat{B}(I - A) - I, \quad \|Z\|_{\max} \leq \lambda_s, \quad h(A) = 0. \quad (10)$$

This reformulation separates the non-smooth constraint from the acyclicity constraint and facilitates efficient optimization.

We solve (10) using an augmented Lagrangian approach combined with the alternating direction method of multipliers (ADMM). Introducing a dual variable $V \in \mathbb{R}^{p \times p}$ for the linear constraint $Z = \hat{B}(I - A) - I$, the augmented Lagrangian is given by

$$\mathcal{L}_\rho(A, Z, V) = \|A\|_1 + \alpha h(A) + \frac{\mu}{2} h(A)^2 + \frac{\rho}{2} \|Z - (\hat{B}(I - A) - I) + \frac{V}{\rho}\|_F^2 - \frac{1}{2\rho} \|V\|_F^2, \quad (11)$$

where $\rho > 0$ is the ADMM penalty parameter, and $\alpha, \mu > 0$ are the Lagrange multiplier and quadratic penalty coefficient associated with the acyclicity constraint $h(A) = 0$.

ADMM Updates. Given the augmented Lagrangian (11), the ADMM iterations proceed by alternating updates of the primal variables Z and A , followed by a dual update of V . At iteration $t + 1$, the updates are:

$$\begin{aligned}
Z^{(t+1)} &= \Pi_{\|\cdot\|_{\max} \leq \lambda_s}(\widehat{B} - \widehat{B}A^{(t)} - I - \frac{1}{\rho}V^{(t)}), \\
A^{(t+1)} &= \arg \min_A \frac{\rho}{2} \|\widehat{B}A - C^{(t+1)}\|_F^2 + \alpha h(A) + \frac{\mu}{2} h(A)^2 + \|A\|_1, \\
&\text{where } C^{(t+1)} = \widehat{B} - I - Z^{(t+1)} - \frac{1}{\rho}V^{(t)}, \\
V^{(t+1)} &= V^{(t)} + \rho(Z^{(t+1)} - (\widehat{B} - \widehat{B}A^{(t+1)} - I)).
\end{aligned} \tag{12}$$

Here $\Pi_{\|\cdot\|_{\max} \leq \lambda_s}$ denotes the elementwise projection onto the ℓ_∞ ball of radius λ_s , implemented via elementwise truncation to $[-\lambda_s, \lambda_s]$. The update of $A^{(t)}$ is convex apart from the acyclicity constraint and is solved using a proximal gradient method. The iteration terminates when the primal and dual residual norms, relative change in A , and the acyclicity violation $|h(A)|$ fall below prespecified tolerances. More implementation details are provided in Supplementary Material Section A.1.

Choice of λ_s . The sparsity parameter λ_s is selected using a pseudo-BIC (PBIC) criterion.

For each candidate λ_s , we define the criterion

$$\text{PBIC}(\lambda_s) = \frac{\|\widehat{B}(I - \widehat{A}(\lambda_s)) - I\|_F^2}{\|\widehat{B} - I\|_F^2} + C_w \cdot \frac{\|\widehat{A}(\lambda_s)\|_0}{p(p-1)/2}, \tag{13}$$

where $C_w > 0$ controls the trade-off between model fit and sparsity. In our implementation we set $C_w = 2$ and select λ_s by minimizing $\text{PBIC}(\lambda_s)$ over a grid of candidate values.

5 Theoretical Properties

In this section, we investigate the estimation error of the causal coefficient matrix and the graph recovery consistency for the proposed estimator in Section 4. We first introduce additional notations.

Let $A^* \in \mathbb{R}^{p \times p}$ denote the true coefficient matrix of the latent Gaussian structural causal model, $B^* := (I - A^*)^{-1}$, and $\mathcal{G}^* = \mathcal{G}(A^*)$. Let $\mu^{(m)*} = B^* \eta^{(m)}$ denote the true latent mean. For $\tau > 0$, define the entrywise hard-thresholded matrix A_τ by $(A_\tau)_{ij} := a_{ij} \mathbf{1}\{|a_{ij}| \geq \tau\}$, $1 \leq i, j \leq p$. Define $n_{\min} = \min_{m \in [p] \cup \{0\}} n_m$. We make the following assumptions.

Assumption 5.1 (Moments). *Suppose there exist some constants $r, c, \delta, c_{\min} > 0$ such that (i) $p \leq cn^r$, (ii) $\mathbb{E}|Y_j^{(m)}|^{4+8r+\delta} \leq K$, and (iii) $\mathbb{E}[Y_j^{(m)}] \geq c_{\min}$ for $j \in [p]$ and $m \in [p] \cup \{0\}$.*

Assumption 3.1 imposes moment conditions on the scaled observed Poisson counts to ensure well-behaved concentration of moment estimators. It is mild for Poisson-lognormal models, as Gaussian latent variables imply finite moments for the Poisson rates and the scaled counts; similar conditions are standard in related work (Cai et al., 2011; Xiao et al., 2022). The lower bound $\mathbb{E}[Y_j^{(m)}] \geq c_{\min}$ excludes degenerate variables and ensures stable moment estimation.

Assumption 5.2 (Mean Shift Strength). *Let $t > 0$ be some small constant. Assume that the strength of the mean shift is strong enough, that is, $\min_{m \in [p]} |\alpha_m| \geq \Delta_{\min}$, where $\Delta_{\min} \geq c_1 \sqrt{\log p / n_{\min}}$ and $c_1 = 8\sqrt{(2K + 1)(t + 3)}$.*

Assumption 3.2 specifies a minimal intervention strength for finite-sample identifiability, serving as a finite-sample counterpart of population-level mean-shift conditions in literature of intervention-based causal discovery. The requirement $\Delta_{\min} \gtrsim \sqrt{\log p / n_{\min}}$ matches the intrinsic noise level and is therefore statistically necessary. Moreover, it is empirically verifiable since $\Delta \mu_{\ell_m}^{(m)}$ can be estimated from sample means across environments.

The following lemma establishes a uniform tail bound for the estimation error of the sample means across all variables and environments.

Lemma 5.1. *Under Assumption 5.1, it holds that*

$$P \left(\max_{m,j} |\hat{\mu}_j^{(m)} - \mu_j^{(m)*}| \geq \frac{c_1}{4c_{\min}} \sqrt{\frac{\log p}{n_{\min}}} \right) = O(n_{\min}^{-\frac{\delta}{4}} + p^{-r}).$$

Theorem 5.2 provides finite-sample error bounds for estimating the latent causal coefficient matrix A^* under interventional Poisson count data. The entrywise bound $\|\hat{A} - A^*\|_{\max} = O\left((c_{\min}\Delta_{\min})^{-1}\sqrt{\log p/n_{\min}}\right)$ is the key rate for edge-wise accuracy and support recovery, while the spectral and Frobenius bounds further quantify global estimation error under weak row-sparsity $s_0(p)$ for $q \in [0, 1)$. The appearance of Δ_{\min} in the denominator reflects the impact of mean-shift signal strength on estimating the coefficient matrix A , as weaker mean shifts reduce the separability between control and interventional data and necessarily inflate the estimation error. The dependence on $s_0(p)$ captures the effect of graph density, with larger $s_0(p)$ corresponding to denser underlying graphs and leading to increased estimation error in the spectral and Frobenius norms.

Theorem 5.2 (Estimation). *Assume that $\|I - A^*\|_{L_1} \leq M$ for some large $M > 0$ and A^* is weakly sparse in the sense that $\max_j \sum_{k=1}^p |a_{jk}^*|^q \leq s_0(p)$ for some $0 \leq q < 1$. Under Assumptions 5.1 and 5.2, and by choosing $\lambda_s = c_1 M / (c_{\min} \Delta_{\min}) \sqrt{\log p / n_{\min}}$, it holds that*

$$\begin{aligned} \|\hat{A} - A^*\|_{\max} &\leq \frac{4c_1 M^2}{c_{\min} \Delta_{\min}} \sqrt{\frac{\log p}{n_{\min}}}, \\ \|\hat{A} - A^*\|_2 &\leq c_2 (4M)^{1-q} \left(\frac{c_1 M}{c_{\min} \Delta_{\min}} \sqrt{\frac{\log p}{n_{\min}}} \right)^{1-q} s_0(p), \\ \frac{\|\hat{A} - A^*\|_F^2}{p} &\leq c_2 (4M)^{2-q} \left(\frac{c_1 M}{c_{\min} \Delta_{\min}} \sqrt{\frac{\log p}{n_{\min}}} \right)^{2-q} s_0(p), \end{aligned}$$

with probability greater than $1 - O(n_{\min}^{-\delta/4} + p^{-t})$, where $c_2 = 1 + 2^{1-q} + 3^{1-q}$.

To characterize the reconstructability of the underlying DAG, we define the index

$$\zeta := \zeta(A^*) = \inf_{A: \mathcal{G}(A_\tau) \neq \mathcal{G}^*, h(A) = 0, \|A\|_1 \leq \|A^*\|_1} \|B^*(I - A) - I\|_{\max}.$$

The index $\zeta(A^*)$ measures the minimal separation between the true model and any alternative coefficient matrix whose thresholded graph differs from \mathcal{G}^* , and is closely related in spirit to the degree of reconstructability introduced in Yuan et al. (2019).

Assumption 5.3 (DAG Reconstructability). *Assume that $\zeta \geq c_3 \sqrt{\log p/n_{\min}}$, where $c_3 = (c_1 + 2\sqrt{2})M/(c_{\min}\Delta_{\min})$.*

Define $a_{\min} := \min_{(j,k):A_{jk}^* \neq 0} |A_{jk}^*|$. A sufficient condition for Assumption 5.3 is that $a_{\min} \geq 2\tau$ and $\tau \geq (1 + M)c_3 \sqrt{\log p/n_{\min}}$, where τ is the hard-threshold level. It is essentially a beta-min type condition similarly used in (Cai et al., 2011; van de Geer and Bühlmann, 2013; Yuan et al., 2019; Park and Park, 2019).

Remark 5.1. *We remark that the beta-min condition is not directly comparable to the strong faithfulness assumption; the former is a local signal strength condition commonly used in high-dimensional settings, whereas the latter is a global distributional assumption. See van de Geer and Bühlmann (2013) for detailed discussion.*

Theorem 5.3 (Graph Recovery). *Denote $\kappa = (\zeta - \lambda_s)c_{\min}\Delta_{\min}/M$ where λ_s is defined in Theorem 5.2. Under Assumptions in Theorem 5.2, it holds that*

$$P(\hat{\mathcal{G}} = \mathcal{G}^*) > P(\text{sign}(\hat{A}_\tau) = \text{sign}(A^*)) > 1 - c_4 \exp\left(-\frac{n_{\min}}{4} \min\left\{\frac{\kappa^2}{K}, 3\kappa \sqrt{\frac{(\log p)^3}{n_{\min}}}\right\} + 2 \log p\right),$$

for some constant $c_4 > 4$. Further, under Assumption 5.3 and as $n_{\min} \rightarrow \infty$, we have

$$P(\hat{\mathcal{G}} = \mathcal{G}^*) > P(\text{sign}(\hat{A}_\tau) = \text{sign}(A^*)) \rightarrow 1.$$

Theorem 5.3 establishes finite-sample recovery of the latent causal DAG via thresholding the estimated coefficient matrix. The convergence probability is governed by the degree of DAG reconstructability ζ and the mean-shift strength Δ_{\min} through κ : larger values of either quantity accelerate convergence of $P(\hat{\mathcal{G}} = \mathcal{G}^*)$ to one, while weaker reconstructability or mean shifts slow down recovery.

6 Simulation Evaluations

6.1 Setup

Data generation. We consider a mean-shift setting of the latent linear Gaussian structural model described in Section 2, and examine the performance of different methods under different graph densities and mean-shift strengths.

The underlying causal mechanism A was generated from an Erdős–Rényi model under a random topological ordering to ensure acyclicity. For each ordered pair of nodes $i < j$, a directed edge $i \rightarrow j$ was added independently with probability such that the expected average node degree of d , where $d = 2$ for the low-density setting and $d = 2$ for the high-density setting. Nonzero edge weights were drawn uniformly from $\pm[0.3, 0.6]$.

The intercept vector in the control data was fixed as $\eta^{(0)} = (-0.5, \dots, -0.5)$. For interventional data, we consider setting the mean shift strength at different levels, $\alpha_m \in \{-2, -4\}$. Library sizes were sampled independently as $L_i \sim \text{Lognormal}(\log 10, 0.1^2)$. For simplicity, no additional covariates C_i were included.

To introduce latent confounding, we consider pervasive low-rank confounders by setting the number of unmeasured factors to $n_{\text{uc}} = 2$ and generating a loading matrix $U \in \mathbb{R}^{p \times n_{\text{uc}}}$ with i.i.d. entries from $\mathcal{N}(0, \sigma_c^2)$, where σ_c controls the confounding strength. The noise covariance in all environments is specified as $\Sigma_e^{(0)} = \text{diag}(\text{Uniform}(0.5, 0.8)) + UU^\top$, where the low-rank term UU^\top induces residual correlations across genes. We consider $\sigma_c \in \{0, 0.25, 0.5\}$, graph dimension $p \in \{50, 100\}$, control sample size $n_0 = 5000$, and interventional sample size $n_m \in \{100, 200, 500\}$ for each $m \in [p]$.

Competing methods. We compare the proposed methods with a range of existing approaches for DAG learning. NOTEARS (Zheng et al., 2018a), LiNGAM (Shimizu et al.,

2006), and MRS-PoissonSEM (Park and Park, 2019) estimate DAGs from observational data, among which MRS-PoissonSEM is specifically designed for Poisson count data, while the others rely on continuous-valued assumptions. DOTEARS (Xue et al., 2025), GIES (Hauser and Bühlmann, 2012), and IGSP (Wang et al., 2017) leverage interventional data for causal identification. Anchor-PLN-PC (Saeed et al., 2020) accommodates the Poisson log-normal model while explicitly accounting for measurement error and sample heterogeneity. It first estimates an undirected dependency graph and then applies the PC algorithm to recover the corresponding Markov equivalence class of the underlying DAG. Finally, PLN-intervn is the proposed method that exploits interventional Poisson log-normal data.

The proposed methods and Anchor-PLN-PC explicitly model library size effects and were thus applied directly to the raw count data. For competing methods without an explicit library size component, counts were first normalized by the library size L . Furthermore, except for MRS-Poisson-SEM, methods based on approximate continuous assumptions were applied to $\log(1 + x)$ -transformed normalized counts.

For all methods, the estimated adjacency matrix \hat{A} was thresholded at $\tau = 0.01$, yielding \hat{A}_τ as the final estimate. Additional simulations examining sensitivity to different thresholds are reported in Supplementary Material Section A.2.

Evaluation metrics. To assess graph recovery performance, we evaluate edge-level accuracy using precision, recall, and the F1 score, and structural accuracy using the Structural Hamming Distance (SHD). Let TP, FP, FN, and TN denote the numbers of true positives, false positives, false negatives, and true negatives of the directed edge estimation. The precision and recall are defined as $\text{Precision} = \text{TP}/(\text{TP} + \text{FP})$, and $\text{Recall} = \text{TP}/(\text{TP} + \text{FN})$. The F1 score is the harmonic mean of precision and recall,

$$\text{F1} = \frac{2 \text{Precision} \times \text{Recall}}{\text{Precision} + \text{Recall}} = \frac{2 \text{TP}}{2 \text{TP} + \text{FP} + \text{FN}},$$

which provides an edge-level measure of graph recovery accuracy by balancing false discoveries and missed edges. The structural Hamming distance (SHD) is a global metric that counts the number of edge additions, deletions, and reversals needed to transform the estimated graph into the true graph, with smaller values indicating more accurate recovery.

6.2 Results

We report in the main paper the F1 score and SHD under moderate latent confounding ($\sigma_c = 0.25$) with graph dimension $p = 50$. Additional results are deferred to Supplementary Material Section A.2, including Precision and Recall under this setting, robustness to different confounding levels, simulations in higher dimensions, and sensitivity to threshold choices. Figures 1 and 2 summarize the performance of different methods across varying graph densities, mean-shift strengths, and interventional sample sizes, measured by F1 score and SHD, respectively. We highlight several key observations below.

First, the performance of the proposed method improves systematically with stronger mean shifts, lower graph density, and larger interventional sample sizes, as reflected by higher F1 scores and lower SHD. These trends are consistent with the theoretical results in Theorem 5.3, where larger mean-shift strength Δ_{\min} , larger sample size n_{\min} , and smaller $M = \|I - A^*\|_{L_1}$ lead to faster convergence of the estimated graph to the true DAG.

Second, compared with observational-data-based methods, PLN-intervn consistently outperforms NOTEARS, LiNGAM, and MRS-Poisson-SEM across nearly all regimes in terms of both F1 score and SHD. In more challenging settings characterized by high graph density and weak mean shifts, MRS-Poisson-SEM can achieve slightly higher F1 scores than the proposed method when the interventional sample size is small. However, this marginal advantage disappears once the interventional sample size becomes moderate. Moreover,

sensitivity analysis in Supplementary Material Section A.2.5 shows that MRS-Poisson-SEM is much more sensitive to the threshold τ than our method, and the reported results use a τ favorable to MRS-Poisson-SEM.

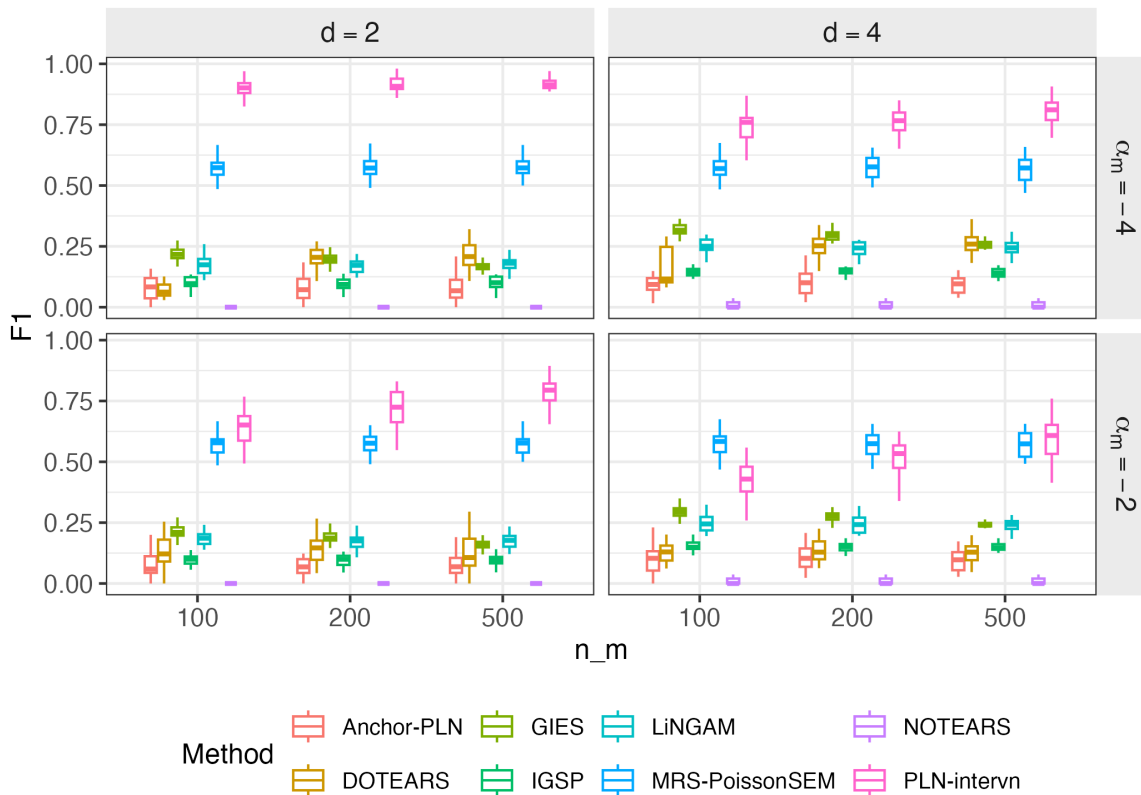


Figure 1: F1 score of different methods under different graph densities, different mean shift strengths, and varying sample sizes of interventional data.

Third, we observe that in this setting, the interventional-data-based methods, including DOTEARS, GIES, and IGSP, can even underperform the observation-based MRS-Poisson-SEM. This phenomenon may be attributed to two factors. First, these methods are primarily designed for hard or do-type interventions, and their performance may degrade under the soft mean-shift interventions considered here. Second, these approaches do not explicitly model the count-valued nature of the data, which can lead to inferior performance compared to MRS-Poisson-SEM, despite the latter relying only on observational

data. This observation further highlights the importance of appropriately modeling count data in causal discovery for perturbation studies.

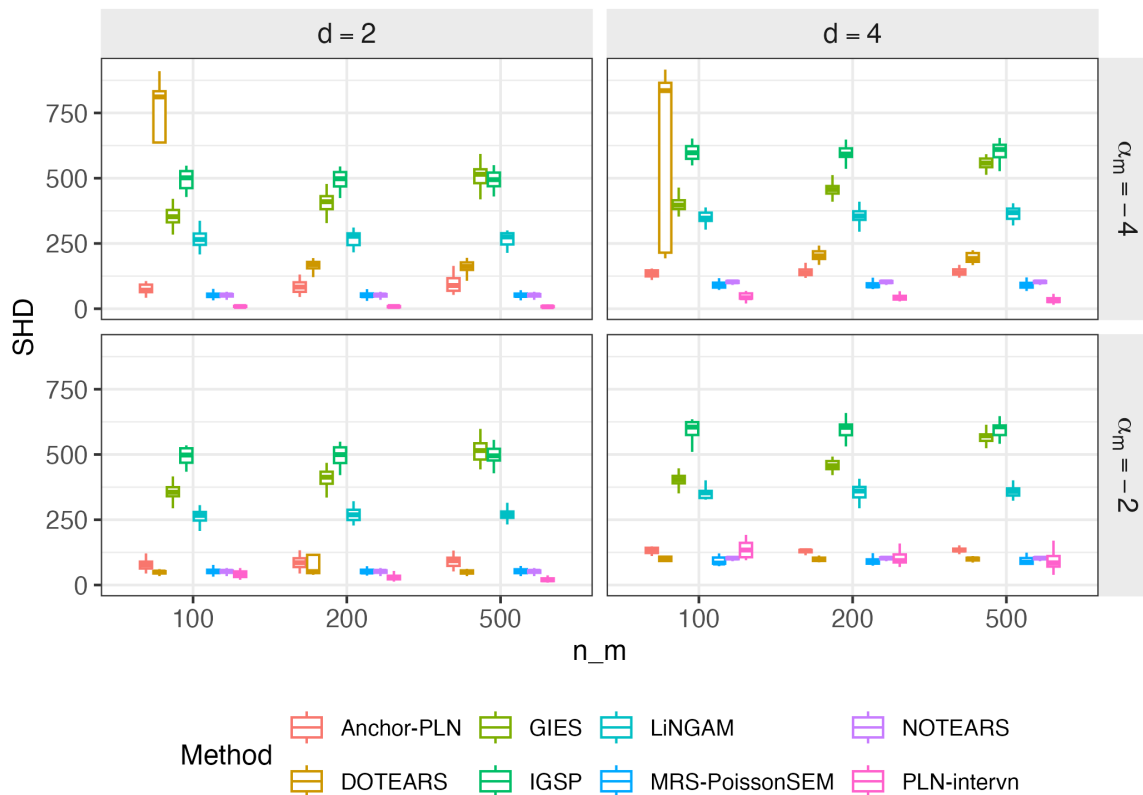


Figure 2: SHD of different methods under different graph densities, different mean shift strengths, and varying sample sizes of interventional data.

Finally, although Anchor-PLN-PC explicitly accounts for count-valued data and measurement error, its F1 score remains relatively low in our simulations. A potential explanation is that the PC algorithm requires estimating the covariance matrix of the latent variables in (2), which can be unstable in high-dimensional settings. Moreover, even with a reliable covariance estimate, PC-based methods are only guaranteed to recover a Markov equivalence class. In contrast, by leveraging interventional data, the proposed method is able to identify the full causal DAG, leading to improved structural recovery.

7 Application to Perturb-seq dataset

We analyze a single-cell CRISPR perturbation dataset from the Perturb-seq study of Replogle et al. (2022), focusing on the K562 chronic myelogenous leukemia cell line. In this experiment, K562 cells expressing a CRISPR interference (CRISPRi; dCas9–KRAB) system were subjected to pooled perturbations targeting approximately 2,000–2,500 essential genes. These genes are defined as those required for cell viability and proliferation, and are enriched for core cellular processes such as transcription, translation, RNA processing, and cell cycle regulation. Single-cell RNA sequencing with guide capture was used to link each perturbation to its transcriptomic response, enabling systematic characterization of gene regulatory effects at single-cell resolution.

After preprocessing to remove genes with insufficient perturbed-cell counts, extreme sparsity, or weak perturbation effects, 794 genes remain, of which we retain the 200 most variable genes in control cells for our analysis. The resulting dataset contains 10,691 control cells and an average of 194 perturbed cells per intervention, with a minimum of 101 perturbed cells per gene.

To construct a biologically informed reference graph, we employed a transcription factor–target interaction network derived from ChIP-seq data (Chevalley et al., 2025), with interactions restricted to those relevant to or observed in the K562 cell line. Within the selected 200 genes, this reference network contains 638 directed edges, with a graph density 0.016. We compare the proposed method with the competing approaches described in Section 6. Detailed preprocessing and implementation steps are provided in Supplementary Material Section B.1.

The ChIP-seq–derived transcription factor–target network provides a useful but inherently limited reference for evaluating the learned DAG from perturb-seq data. While it

offers independent evidence of regulatory relationships, it reflects physical TF–DNA binding rather than functional or causal effects on gene expression. Thus, agreement supports biological plausibility, particularly for direct interactions, whereas discrepancies may arise from context-specific regulation, indirect effects captured by perturb-seq, or incomplete and noisy ChIP-seq coverage. Accordingly, this comparison should be viewed as a complementary, rather than definitive, validation of causal structure.

7.1 Global recovery

Figure 3 presents the precision and recall of different methods as functions of the threshold parameter τ applied to \hat{A}_τ , with τ varying from 0.15 to 0.001 in steps of 0.001. For constraint-based methods, including IGSP and Anchor-PLN, the significance level is fixed at 0.05, and the results are shown as single points. The left vertical axis reports precision and the right vertical axis reports recall. Supplementary Material Section B.4 provides a complementary node-level evaluation, where precision and recall are computed separately for each source gene.

Figure 3 reveals three main findings. First, the proposed method consistently achieves the highest precision across the entire range of thresholds, with its precision curve uniformly dominating those of all competing methods. When $\tau < 0.1$, its recall also substantially exceeds that of other approaches. In contrast, competing methods fail to surpass the density baseline in precision and exhibit limited recall. These results suggest that the proposed method more effectively exploits interventional information to recover regulatory edges.

Second, among the competing approaches, MRS-PoissonSEM and IGSP perform comparatively better than others. MRS-PoissonSEM attains slightly higher precision within a narrow threshold range, whereas IGSP achieves higher recall. LiNGAM, DOTEARS, and

NOTEARS exhibit moderate precision but generally low recall, while Anchor-PLN fails to identify edges on this dataset.

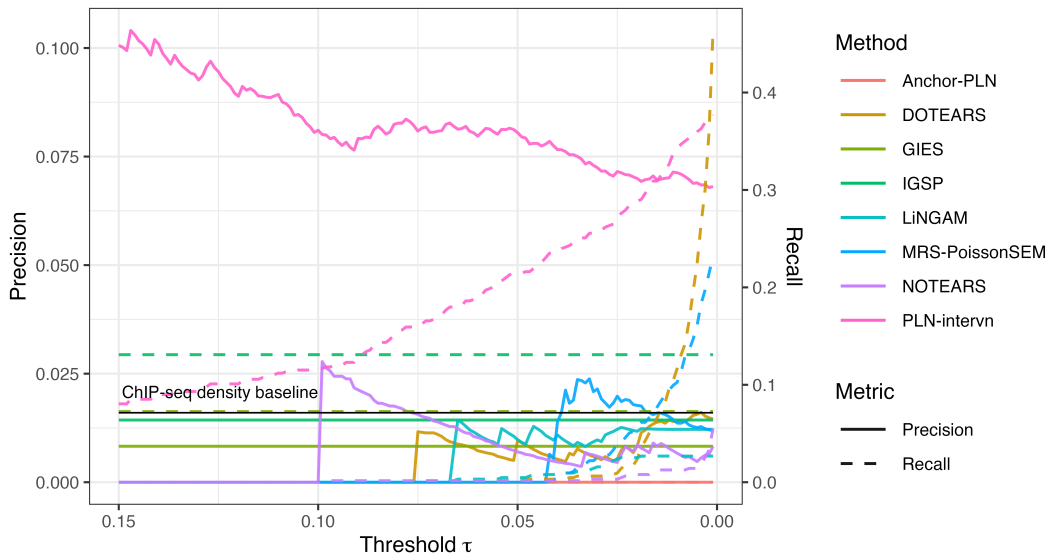


Figure 3: Precision-Recall curves of different methods on ChIP-seq dataset.

Third, the proposed method demonstrates relatively stable behavior with respect to threshold variation. As the threshold decreases, recall increases substantially and steadily while precision remains largely stable. Conversely, as the threshold increases, precision gradually improves, indicating that edges selected under stricter thresholds tend to be more informative and reliable. In contrast, methods such as MRS-PoissonSEM and DOTEARS are relatively more sensitive to threshold choice.

7.2 Distributional shifts in downstream and upstream genes

To examine whether the inferred causal directions are supported by interventional responses, we analyzed distributional shifts following gene perturbations based on the estimated causal graph $\mathcal{G}(\hat{A}_\tau)$ by different methods. For each perturbed gene, we identified its upstream (ancestors) and downstream (descendants) genes according to the directed

structure of $\mathcal{G}(\hat{A}_\tau)$. We use $\tau = 0.15$ for the proposed method and $\tau = 0.03$ for the competing methods, selected based on Figure 3 to balance precision and recall and maintain comparable network sparsity. We then performed two-sample Kolmogorov–Smirnov (KS) tests comparing gene expression between the corresponding perturbation environment and the control condition for all other genes, and partitioned the resulting KS p -values into upstream and downstream groups. Under a correctly inferred causal structure, downstream genes are expected to exhibit stronger distributional shifts, reflected by smaller KS p -values.

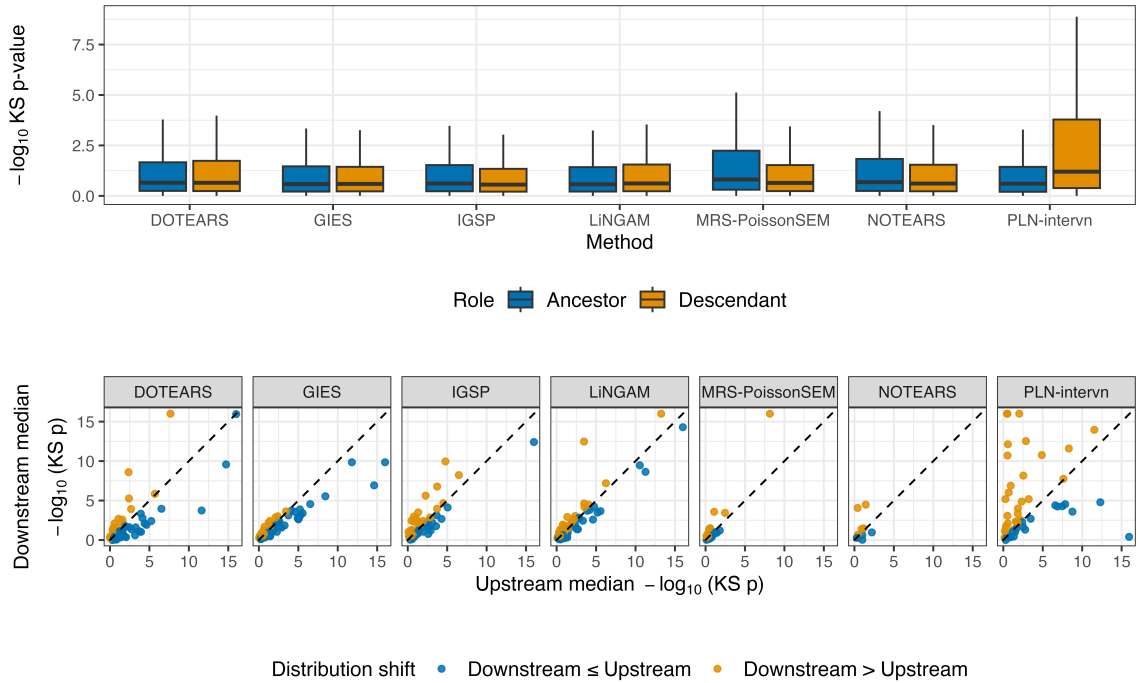


Figure 4: Distributional shifts quantified by $-\log_{10} p$ -values from two-sample Kolmogorov–Smirnov (KS) tests comparing perturbed and control conditions. Upstream (ancestors) and downstream (descendants) genes are defined according to the estimated causal graph $\mathcal{G}(\hat{A}_\tau)$ obtained from obtained from seven different methods. The upper panel pools all gene–perturbation pairs and the lower panel summarizes medians at the perturbation level.

Figure 4 presents the results for different methods at two complementary levels. The

upper panel pools all perturbation–gene pairs and compares the distributions of $-\log_{10}$ KS p -values between downstream and upstream genes for each method. For the proposed method, downstream genes display larger values than upstream genes, indicating stronger perturbation-induced shifts. In contrast, for alternative methods, the separation between downstream and upstream distributions is substantially weaker. Notably, for MRS-PoissonSEM, upstream genes exhibit slightly larger $-\log_{10}$ KS p -values than downstream genes on average, suggesting reversal or misidentification of causal directions. This observation is consistent with the network structure shown in Supplementary Section B.3, where MRS-PoissonSEM tends to produce graphs dominated by high in-degree nodes.

The lower panel of Figure 4 further assesses perturbation-level consistency by summarizing each perturbation separately. For each method and perturbation, we compare the median $-\log_{10}$ KS p -values of its downstream and upstream gene sets. Each point corresponds to one perturbation. For the proposed method, most points lie above the diagonal line and are located toward the upper-left region of the panel, indicating that downstream genes consistently exhibit stronger distributional shifts across perturbations. In contrast, for the competing methods, many points cluster near the origin, suggesting weak or indistinguishable distributional differences between upstream and downstream gene sets.

7.3 Inferred gene regulatory network

Figure 5 visualizes the directed gene regulatory network inferred from the estimated coefficient matrix \hat{A}_τ obtained by the proposed PLN-intervn method with threshold $\tau = 0.2$. Each node represents a gene, and each directed edge corresponds to a regulatory relationship inferred from the perturbation data. Node size reflects the total number of incident edges, capturing the overall connectivity of each gene in the network. Node color encodes

the relative balance between outgoing and incoming regulation, quantified by the ratio $d_{\text{out}}/(d_{\text{out}} + d_{\text{in}})$, where d_{out} and d_{in} denote the out-degree and in-degree of the corresponding gene, respectively. Edges highlighted in red indicate regulatory relationships that are supported by the ChIP-seq dataset. We also provide inferred gene regulatory networks by other candidate methods in Supplementary Material Section B.3.

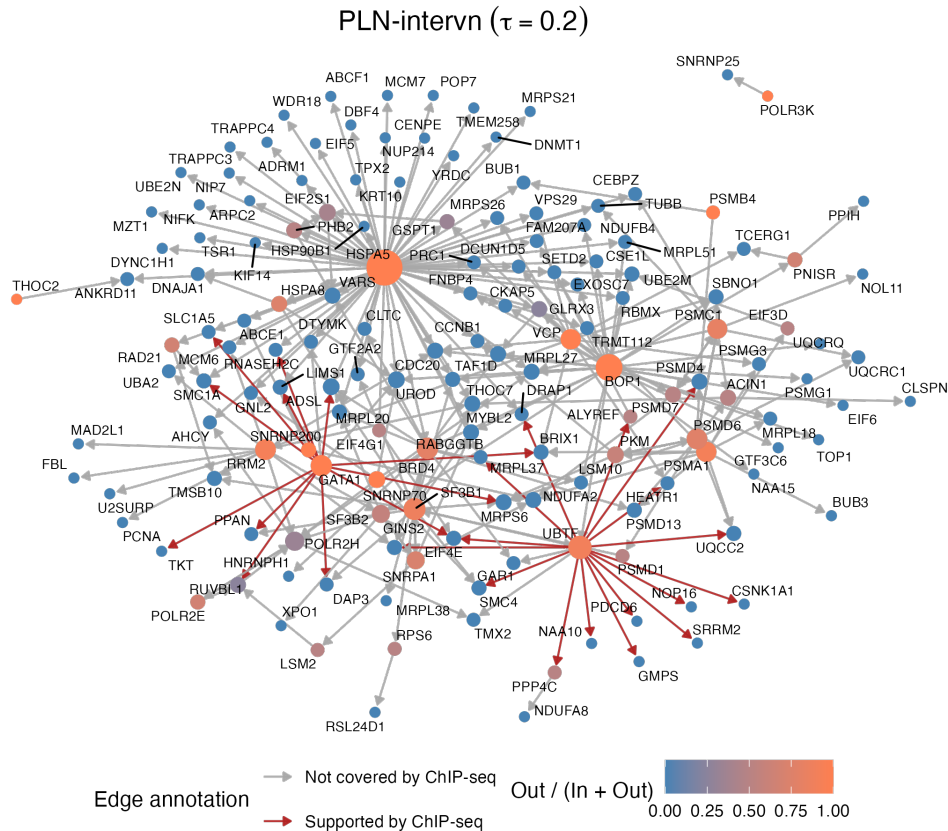


Figure 5: Gene regulatory network inferred by PLN-intervn ($\tau = 0.2$). Node size indicates connectivity, and node color indicates the out-/in-degree ratio.

Inspection of the inferred network reveals a small number of hub genes with markedly large out-degrees, including HSPA5, BOP1, UBTF, GATA1, and SF3B1. Among these, UBTF and GATA1 are well-established transcriptional regulators (Ferreira et al., 2005; Sanij et al., 2015), and many of their outgoing edges are supported by ChIP-seq data, lending support to the biological plausibility of the inferred structure. Notably, among the

relatively few true edges identified by competing methods such as MRS-PoissonSEM and GIES, several outgoing edges from UBTF and GATA1 are also recovered. HSPA5 emerges as the most prominent hub gene, which is biologically plausible given its central role in regulating stress-response and cell-cycle programs. Its strongest inferred target, HSP90B1, is likewise involved in endoplasmic reticulum protein folding, further supporting this regulatory relationship (Steiner, 2022). More detailed biological interpretation is provided in Supplementary Material Section B.2.

8 Discussion

This paper studies causal discovery from interventional count data motivated by single-cell perturbation experiments such as Perturb-seq. These data present key challenges for existing methods, including discrete observations, substantial measurement noise, and latent cellular heterogeneity. Most current approaches assume continuous data with independent noise, limiting their applicability in this setting. We address these challenges by proposing a latent structural framework that separates the causal mechanism on latent gene expression from the Poisson measurement process. Under a mean-shift intervention design, we establish identifiability of the latent causal structure through cross-environment shifts in latent means. We further develop an estimation procedure that combines moment-based recovery of latent mean shifts with sparse DAG estimation, and provide finite-sample guarantees. Simulations and analysis of Perturb-seq data demonstrate improved performance when both count structure and interventional design are properly accounted for.

Several extensions are possible. First, the framework is not limited to the Poisson–lognormal model; it can be extended to other count models, such as zero-inflated or dropout-aware Poisson models (Saeed et al., 2020), provided suitable moment relationships are avail-

able. Second, while we focus on mean-shift interventions, other types may also be informative. In particular, variance-shift interventions that modify the noise covariance, e.g., $\Sigma_e^{(m)} = \Sigma_e^{(0)} + \beta_m e_{\ell_m} e_{\ell_m}^\top$, could enable identification via second-order contrasts, since the leading eigenvector of $\Sigma_e^{(m)} - \Sigma_e^{(0)}$ recovers the ℓ_m -th column of B up to scale. This raises the question of whether identifiability results analogous to Theorem 3.1 can be established in this setting. However, such approaches typically require larger sample sizes to estimate covariance structures reliably, leaving open the question of how to develop methods suitable for small-sample regimes.

Data Availability

The data that support the findings of this study are openly available at <https://gwps.wi.mit.edu>.

Acknowledgements

This research is supported by NIH grants GM129781 and HG013841.

Supplementary Materials

The supplementary material includes additional simulation details and evaluations, detailed results for real data application and all the proofs.

References

Bello, K., B. Aragam, and P. K. Ravikumar (2022). Dagma: Learning directed acyclic graphs with gradient-based methods. In *Proceedings of the 39th International Conference*

on *Machine Learning (ICML)*, pp. 1777–1793. PMLR.

Bhattacharya, R., T. Nagarajan, D. Malinsky, and I. Shpitser (2021). Differentiable causal discovery under unmeasured confounding. In *International Conference on Artificial Intelligence and Statistics*, pp. 2314–2322. PMLR.

Cai, T. T., W. Liu, and X. Luo (2011). Constrained ℓ_1 minimization for sparse precision matrix estimation. *Journal of the American Statistical Association* 106(494), 594–607.

Chevalley, M., Y. H. Roohani, A. Mehrjou, J. Leskovec, and P. Schwab (2025). A large-scale benchmark for network inference from single-cell perturbation data. *Communications Biology* 8(1), 412.

Chickering, D. M. (2002). Optimal structure identification with greedy search. *Journal of machine learning research* 3(Nov), 507–554.

Choi, J. and Y. Ni (2023). Model-based causal discovery for zero-inflated count data. *Journal of Machine Learning Research* 24(200), 1–32.

Colombo, D., M. H. Maathuis, M. Kalisch, and T. S. Richardson (2012). Learning high-dimensional directed acyclic graphs with latent and selection variables. *The Annals of Statistics*, 294–321.

Dai, H., P. Spirtes, and K. Zhang (2022). Independence testing-based approach to causal discovery under measurement error and linear non-gaussian models. *Advances in Neural Information Processing Systems* 35, 27524–27536.

Ferreira, R., K. Ohneda, M. Yamamoto, and S. Philipsen (2005). Gata1 function, a paradigm for transcription factors in hematopoiesis. *Molecular and Cellular Biology* 25(4), 1215–1227.

- Frot, B., P. Nandy, and M. H. Maathuis (2019). Robust causal structure learning with some hidden variables. *Journal of the Royal Statistical Society Series B: Statistical Methodology* 81(3), 459–487.
- Hauser, A. and P. Bühlmann (2012). Characterization and greedy learning of interventional markov equivalence classes of directed acyclic graphs. *The Journal of Machine Learning Research* 13(1), 2409–2464.
- Heinze-Deml, C., M. H. Maathuis, and N. Meinshausen (2018). Causal structure learning. *Annual Review of Statistics and Its Application* 5(1), 371–391.
- Li, J., B. B. Chu, I. F. Scheller, J. Gagneur, and M. H. Maathuis (2025). Root cause discovery via permutations and cholesky decomposition. *Journal of the Royal Statistical Society Series B: Statistical Methodology*, qkaf066.
- Liu, E., J. Zhang, and C. Uhler (2025). Learning genetic perturbation effects with variational causal inference. *bioRxiv*, 2025–06.
- Pal, S., J. O’quinn, K. Aryan, H. Pua, J. P. Long, and A. Asiaee (2025). Dag decoration: Continuous optimization for structure learning under hidden confounding. *arXiv preprint arXiv:2510.02117*.
- Park, G. and S. Park (2019). High-dimensional poisson structural equation model learning via l_1 -regularized regression. *Journal of Machine Learning Research* 20(95), 1–41.
- Park, G. and G. Raskutti (2015). Learning large-scale poisson dag models based on overdispersion scoring. *Advances in neural information processing systems* 28.
- Pearl, J. (2009). *Causality: Models, Reasoning, and Inference* (2 ed.). Cambridge: Cambridge University Press.

- Peters, J. and P. Bühlmann (2014). Identifiability of gaussian structural equation models with equal error variances. *Biometrika* 101(1), 219–228.
- Replogle, J. M., R. A. Saunders, A. N. Pogson, J. A. Hussmann, A. Lenail, A. Guna, L. Mascibroda, E. J. Wagner, K. Adelman, G. Lithwick-Yanai, et al. (2022). Mapping information-rich genotype-phenotype landscapes with genome-scale perturb-seq. *Cell* 185(14), 2559–2575.
- Saeed, B., A. Belyaeva, Y. Wang, and C. Uhler (2020). Anchored causal inference in the presence of measurement error. In *Conference on uncertainty in artificial intelligence*, pp. 619–628. PMLR.
- Sani, E., J. Diesch, A. Lesmana, G. Poortinga, N. Hein, G. Lidgerwood, D. P. Cameron, J. Ellul, G. J. Goodall, L. H. Wong, A. S. Dhillon, N. Hamdane, L. I. Rothblum, R. B. Pearson, I. Haviv, T. Moss, and R. D. Hannan (2015). A novel role for the pol i transcription factor ubtf in maintaining genome stability through the regulation of highly transcribed pol ii genes. *Genome Research* 25(2), 201–212.
- Sarkar, A. and M. Stephens (2021). Separating measurement and expression models clarifies confusion in single-cell rna sequencing analysis. *Nature genetics* 53(6), 770–777.
- Schölkopf, B., F. Locatello, S. Bauer, N. R. Ke, N. Kalchbrenner, A. Goyal, and Y. Bengio (2021). Toward causal representation learning. *Proceedings of the IEEE* 109(5), 612–634.
- Shalem, O., N. E. Sanjana, E. Hartenian, X. Shi, D. A. Scott, T. S. Mikkelsen, D. Heckl, B. L. Ebert, D. E. Root, J. G. Doench, et al. (2014). Genome-scale crispr-cas9 knockout screening in human cells. *Science* 343(6166), 84–87.
- Shen, X., P. Bühlmann, and A. Taeb (2025). Causality-oriented robustness: exploiting

- general noise interventions in linear structural causal models. *Journal of the American Statistical Association* (just-accepted), 1–20.
- Shimizu, S., P. O. Hoyer, A. Hyvärinen, and A. Kerminen (2006). A linear non-gaussian acyclic model for causal discovery. *Journal of Machine Learning Research* 7, 2003–2030.
- Spirtes, P., C. N. Glymour, and R. Scheines (2000). *Causation, prediction, and search*. MIT press.
- Squires, C. and C. Uhler (2023). Causal structure learning: A combinatorial perspective. *Foundations of Computational Mathematics* 23(5), 1781–1815.
- Squires, C., Y. Wang, and C. Uhler (2020). Permutation-based causal structure learning with unknown intervention targets. In *Conference on Uncertainty in Artificial Intelligence*, pp. 1039–1048. PMLR.
- Steiner, L. A. (2022). Helping gata1 make complex decisions. *Blood* 139(24), 3457–3459.
- Uhler, C., G. Raskutti, P. Bühlmann, and B. Yu (2013). Geometry of the faithfulness assumption in causal inference. *The Annals of Statistics*, 436–463.
- van de Geer, S. and P. Bühlmann (2013). ℓ_0 -penalized maximum likelihood for sparse directed acyclic graphs. *The Annals of Statistics* 41(2), 536–567.
- Varici, B., E. Acartürk, K. Shanmugam, A. Kumar, and A. Tajer (2025). Score-based causal representation learning: Linear and general transformations. *Journal of Machine Learning Research* 26(112), 1–90.
- Wang, Y., L. Solus, K. D. Yang, and C. Uhler (2017). Permutation-based causal inference algorithms with interventions. In *Proceedings of the 31st International Conference on*

Neural Information Processing Systems, NIPS'17, Red Hook, NY, USA, pp. 5824–5833.

Curran Associates Inc.

Wang, Y. S. and M. Drton (2023). Causal discovery with unobserved confounding and non-gaussian data. *Journal of Machine Learning Research* 24(271), 1–61.

Xiao, F., J. Tang, H. Fang, and R. Xi (2022). Estimating graphical models for count data with applications to single-cell gene network. *Advances in Neural Information Processing Systems* 35, 29038–29050.

Xue, A., J. Rao, S. Sankararaman, and H. Pimentel (2025). dotears: Scalable and consistent directed acyclic graph estimation using observational and interventional data. *iScience* 28(2).

Yuan, Y., X. Shen, W. Pan, and Z. Wang (2019). Constrained likelihood for reconstructing a directed acyclic gaussian graph. *Biometrika* 106(1), 109–125.

Zhang, K., M. Gong, J. D. Ramsey, K. Batmanghelich, P. Spirtes, and C. Glymour (2018). Causal discovery with linear non-gaussian models under measurement error: Structural identifiability results. In *UAI*, pp. 1063–1072.

Zheng, X., B. Aragam, P. Ravikumar, and E. P. Xing (2018a). Dags with no tears: continuous optimization for structure learning. NIPS'18, Red Hook, NY, USA, pp. 9492–9503. Curran Associates Inc.

Zheng, X., B. Aragam, P. K. Ravikumar, and E. P. Xing (2018b). Dags with no tears: Continuous optimization for structure learning. In *Advances in Neural Information Processing Systems (NeurIPS)*, Volume 31, pp. 9472–9483.